Journal of
Synchrotron
Radiation

ISSN 0909-0495

Received 25 May 2010
Accepted 6 July 2010

Synchrotron PEEM and ToF-SIMS study of oxidized heterogeneous pentlandite, pyrrhotite and chalcopyrite

Robert George Acres, Sarah Louise Harmer and David Allan Beattie*

Ian Wark Research Institute, University of South Australia, Australia.
E-mail: david.beattie@unisa.edu.au

Synchrotron-based photoemission electron microscopy (PEEM; probing the surface region) and time-of-flight secondary ion mass spectrometry (ToF-SIMS; probing the uppermost surface layer) have been used to image naturally heterogeneous samples containing chalcopyrite ($CuFeS_2$), pentlandite [$(Ni,Fe)_9S_8$] and monoclinic pyrrhotite (Fe_7S_8) both freshly polished and exposed to pH 9 KOH for 30 min. PEEM images constructed from the metal L_3 absorption edges were acquired for the freshly prepared and solution-exposed mineral samples. These images were also used to produce near-edge X-ray absorption fine-structure spectra from regions of the images, allowing the chemistry of the surface of each mineral to be interrogated, and the effect of solution exposure on the mineral surface chemistry to be determined. The PEEM results indicate that the iron in the monoclinic pyrrhotite oxidized preferentially and extensively, while the iron in the chalcopyrite and pentlandite underwent only mild oxidation. The ToF-SIMS data gave a clearer picture of the changes happening in the uppermost surface layer, with oxidation products being observed on all three minerals, and significant polysulfide formation and copper activation being detected for pyrrhotite.

Keywords: PEEM; sulfide mineral; oxidation; ToF-SIMS; heterogeneity; chalcopyrite; pyrrhotite; pentlandite.

1. Introduction

Ores that are mined for the extraction of metals contain many different minerals, not all of which are valuable. One of the most common means to separate valuable minerals from worthless minerals is the process of flotation. Flotation exploits differences in surface hydrophobicity to selectively separate the valuable minerals in an ore from the worthless mineral phases. The process involves passing gas bubbles through a suspension of the ground ore. Hydrophobic particles attach to the rising bubbles and are brought to the surface where they are skimmed off and collected, while hydrophilic particles remain in suspension (Wills & Napier-Munn, 2005). Ores containing valuable metal sulfide minerals are commonly processed in this manner.

The surface chemistry of sulfide minerals is crucial to their effective flotation and separation from the associated worthless minerals. Oxidation in particular is an important process affecting sulfide floatability and selectivity (oxidation products can either enhance or diminish hydrophobicity); consequently the oxidation of sulfide minerals under processing related conditions has received a great deal of research attention. Metal sulfide minerals oxidize by diffusion of metal ions from the near surface layers to the surface where they oxidize to form a metal hydroxide, also resulting in a metal-depleted, sulfur-rich layer (Grano *et al.*, 1997; Vaughan *et al.*, 1997; Yin *et al.*, 1995, 2000; Fairthorne *et al.*, 1997; Todd *et al.*, 2003; Mielczarski *et al.*, 1996; Parker *et al.*, 2005; Harmer *et al.*, 2006).

Conventional X-ray photoemission spectroscopy (XPS) has been used in the study of mineral oxidation for some time (Buckley, 1994; Buckley & Woods, 1984; Brion, 1980). The improved resolution and surface sensitivity that synchrotron radiation affords XPS has been exploited to gain an even better understanding of mineral surface chemistry and the processes that occur on their surfaces, especially the initial state of the surface after fracture (Harmer *et al.*, 2004, 2005, 2009; Buckley *et al.*, 2007; Pratt, 2004). Oxidation states, the oxidation process and its effects on flotation have all been studied by synchrotron-based XPS (Harmer *et al.*, 2006; Acres *et al.*, 2010*a*,*b*; Laajalehto *et al.*, 1997; Buckley *et al.*, 2003) and also near-edge X-ray absorption fine structure (NEXAFS) (Goh *et al.*, 2006*a*,*c*,*d*; Mikhlin & Tomashevich, 2005; Buckley *et al.*, 2007).

Photoemission electron microscopy (PEEM) is a synchrotron technique that has not yet been applied to the study of sulfide mineral oxidation, in spite of it offering significant

benefits over bulk NEXAFS for composite/heterogeneous materials. The advantages of PEEM for such studies are that it provides surface chemical imaging as well as chemical state and bonding information. Imaging is critical as a surface's hydrophobicity depends not only on the proportion of the hydrophobic and hydrophilic surface species but also on their distribution. While time-of-flight secondary ion mass spectrometry (ToF-SIMS) is able to produce maps of elemental distribution across a mineral surface, it does not provide the same degree of chemical information as XPS or NEXAFS. Imaging conventional XPS does provide chemical imaging, but with a spatial resolution too poor to highlight the different domains in most heterogeneous mineral samples. Only two synchrotron imaging techniques have the surface sensitivity and spatial resolution for flotation-related surface studies of heterogeneous minerals with grains/domains in the micrometre to sub-micrometre range: scanning photoelectron spectroscopy (SPEM) and PEEM. The data produced by PEEM (elemental images as well as NEXAFS spectra from each pixel in the image) have the potential to provide significant insights into the development of sulfide mineral surface chemistry of heterogeneous mineral samples. Another advantage of PEEM is the ability to easily extract data from any given point on the surface, allowing one to investigate how a surface changes with distance from a feature or grain interface. PEEM has been applied to heterogeneous minerals by Smith *et al.* (1998) and Schmidt *et al.* (2001) to image the distribution of mineral phases across natural samples. However, these studies were concerned with identification of mineral phases within heterogeneous samples, rather than the study of surface processes.

In this study, PEEM is applied to polished surfaces of samples containing three metal sulfides: chalcopyrite, pentlandite and pyrrhotite. Chalcopyrite ($CuFeS_2$) and pentlandite [$(Fe,Ni)_9S_8$] are the most significant sources of industrial copper and nickel, respectively (Legrand *et al.*, 1997, 2005; Buckley & Woods, 1984, 1991; Harmer *et al.*, 2004) and are often associated with the iron sulfide pyrrhotite ($Fe_{1-x}S$) (Bozkurt *et al.*, 1998; Newell *et al.*, 2006; Kelebek *et al.*, 1996; Kelebek, 1993; Miller *et al.*, 2005; Kolahdoozan, 2002; Agar, 1991; Yoon *et al.*, 1995). Pyrrhotite is usually considered a worthless minerals phase and separated magnetically or by flotation in order to maximize the grade of nickel ore concentrate and minimize sulfur dioxide emissions during smelting (Bozkurt *et al.*, 1998; Kelebek *et al.*, 1996; Khan & Kelebek, 2004; Kelebek, 1993; Kolahdoozan, 2002; Bozkurt *et al.*, 1999; Agar, 1991; Heiskanen *et al.*, 1991; Senior *et al.*, 1995), but is recovered when processing platinum group mineral ores (Miller *et al.*, 2005; Buswell *et al.*, 2002). In this work the samples have been studied as freshly polished surfaces and polished surfaces oxidized in solution at pH 9, in order to study the development of oxidation products on each mineral phase across the surface, particularly near interfaces between minerals.

The PEEM studies reported in this work are combined with measurements of the same surfaces using ToF-SIMS. ToF-SIMS is a popular tool for studying the changes to mineral surfaces arising from processing-related conditions (Harmer *et al.*, 2008; Khmeleva *et al.*, 2005; Piantadosi *et al.*, 2000; Smart *et al.*, 1998, 2000; Priest *et al.*, 2008; Pratt *et al.*, 1998) and is an ideal complimentary technique to PEEM analysis, given the monolayer sensitivity of the former and the surface-to-bulk sensitivity of the latter. In fact, SIMS has been used previously to study the oxidation of a composite sulfide mineral surface (Pratt *et al.*, 1998), with the study focusing on the degree of hydration of the mineral oxidation products. Our work combines the high surface selectivity of ToF-SIMS with the slightly deeper surface probe of PEEM to give a more complete picture of the development of surface oxidation products on a heterogeneous metal sulfide mineral surface.

2. Experimental

2.1. Minerals and materials

Samples used in this study were cut from a core sample from Frood Mine in the Sudbury Basin, Ontario, Canada. Samples containing all three phases (chalcopyrite, pyrrhotite and pentlandite) were selected and polished. The purity and stoichiometry of the phases in these heterogeneous samples was determined using a CAMECA SX51 electron microprobe operating at 20 kV and 20 nA. Measurements were taken from ten points on each region and averaged: chalcopyrite $CuFeS_{2.05}$; pentlandite $Fe_{4.49}Ni_{3.99}Co_{0.18}S_{8.00}$; pyrrhotite $Fe_{7.00}S_{7.77}$. The stoichiometry of the pyrrhotite in the sample indicates that it is monoclinic and not hexagonal; no significant stoichiometric variation was detected across the area of pyrrhotite analysed. The sample also displayed magnetism, which is characteristic of monoclinic pyrrhotite.

Ultrapure water was produced on a Millipore MilliQ Element system with a resistivity of 18.0 MΩ cm^{-1}. A pH 9 KOH solution was produced by dissolving reagent-grade (>90%) KOH in ultrapure water. The diamond polishing compounds were Struers DP-Stick Ps with particle sizes of 1 μm and 0.25 μm. The silica polishing suspension used was Struers OP-U suspension (particle size 0.04 μm) adjusted to pH 7 using dilute HCl.

2.2. Surface preparation and modification

Samples were cut from the massive sample using a slow diamond saw and then shaped and abraded using 600 then 1200 grit silicon carbide paper, lubricated with ultrapure water. A small amount of 1 μm diamond paste was applied to a Beuhler Trident polishing pad and the sample worked by hand in a figure-8 pattern approximately 4 cm in length, then worked on a clean section of the polishing pad again in a figure-8 pattern. Polishing with 0.25 μm diamond paste followed the same procedure as with the 1 μm paste. Final polishing was carried out with 0.04 μm silica suspension in the same manner as diamond polishing, but on a Struers NAP polishing pad, pre-wetted with ultrapure water. One sample was analysed as fresh polished and the other was oxidized by immersion in pH 9 KOH for 30 min. Polishing of the unoxidized sample was timed to be complete just before the

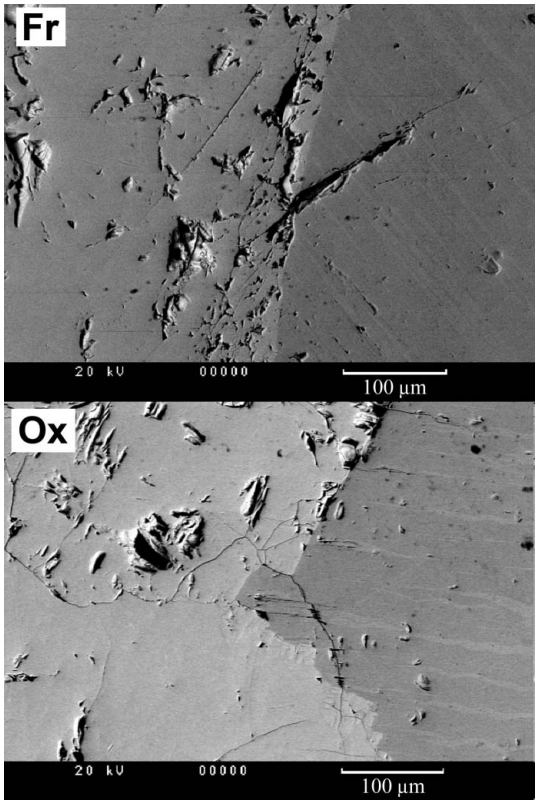

Figure 1
Backscattered electron micrograph of the regions investigated by PEEM on polished composite minerals containing chalcopyrite, pyrrhotite and pentlandite (Fr = sample analysed by freshly polished PEEM; Ox = sample analysed by PEEM after oxidation).

oxidized sample was removed from solution, to enable both to be placed in the PEEM vacuum chamber at the same time. After immersion the oxidized sample was rinsed in clean pH 9 KOH solution to stop solution species from drying onto the surface. Excess rinse solution was removed using lint-free laboratory wipes without touching the surface to be analysed. Backscattered scanning electron (BSE) micrographs of the regions studied by PEEM on the fresh polished and oxidized samples are given in Fig. 1. BSE phase contrast between chalcopyrite and pentlandite was not possible owing to the limitations of the backscatter detector on this instrument.

2.3. Scanning electron microscopy analysis

Scanning electron microscopy and energy dispersive analysis of X-rays (EDAX) were performed on a CamScan 44FE fitted with a field emission electron gun and EDAX detector. A primary electron beam accelerating voltage of 20 kV was used with the spot size set to 10. Micrographs were imaged using the backscatter detector to provide mineral phase contrast. EDAX X-ray maps were collected for copper, iron and nickel by rastering the beam across the surface. In order to confirm phase identity, EDAX spectra were collected from the exact regions imaged with PEEM. EDAX spectra were standardless and collected in spot mode until the peak channel counts were $\sim$10000 with a dead-time ratio of $\sim$45%. EDAX spectra were collected only as an indication of the phases present on the regions probed by PEEM. More accurate determinations of the stoichiometry were determined by electron microprobe analysis before PEEM was conducted.

2.4. PEEM analysis

PEEM experiments were conducted on beamline BL05B2 at the National Synchrotron Radiation Research Centre (NSRRC), Taiwan. BL05B2 uses an elliptically polarized undulator (EPU5) with a spherical-grating monochromator, providing 2×10^{12} photons s^{-1} at 800 eV and a beam of 0.4 mm $\times$ 0.2 mm. Images are generated by collecting the total electron yield (TEY) signal on a phosphor screen mounted on a CCD detector.

Varying the excitation energy across the range of a desired peak generates a stacked PEEM image where each layer represents a discrete excitation energy and the intensity of each pixel represents the TEY signal intensity at that energy for the area of the sample projected onto the pixel. NEXAFS spectra can be derived from specific points on the image from the pixel intensities on each layer. 40 $\times$ 40 pixel regions were analysed to obtain an acceptable signal-to-noise ratio. Copper, nickel and iron spectra were calibrated using metallic standards and published values for the L_3 peak energy [Cu metal 932.6 eV (Goh *et al.*, 2006*d*), Fe metal 707.7 eV (Pearce *et al.*, 2006), Ni metal 852.7 eV (Blanchard *et al.*, 2008; Goh *et al.*, 2006*b*)]. TEY probe depths are up to approximately 12 monolayers, with approximately 40% of the signal originating from the first four monolayers. The NEXAFS spectra energy resolution is as follows: Cu, 0.17 eV (15 μm slit); Ni, 0.14 eV (15 μm slit); Fe, 0.11 eV (15 μm slot). Spectra were normalized such that the height of the peak corresponding to the bulk metal was 1 and the baseline of the pre-edge background was 0.

2.5. ToF-SIMS analysis

ToF-SIMS analysis in this study was conducted on a PHI TRIFT II static SIMS instrument. A Ga^+ liquid-metal ion gun was the primary ion source, operating at a current of 600 pA and 25 kV excitation voltage. Images were collected using a raster size of either 200 $\times$ 200 μm or 100 $\times$ 100 μm. Images were divided into regions of interest approximately 20 $\times$ 20 μm to 30 $\times$ 30 μm in size. Negative ion and positive ion spectra were collected from each individual region of interest (ROI) and normalized to the maximum intensity and averaged over the total number of ROIs for that sample. At least 32 ROIs were defined per sample, from images taken at several points on the sample. ROI boundaries were set within the contrast edges of the regions. The analysis of multiple ROIs allowed for the determination of signal variability and associated confidence intervals (95% probability) for the signal of each surface component (Piantadosi *et al.*, 2000; Piantadosi & Smart, 2002). ToF-SIMS peak intensities vary significantly depending on the surface environment [the matrix effect (Vickerman, 2001)]. As a result of this dependence, ToF-SIMS is not able to quantify the surface composition since no

sensitivity factors exist (as in XPS) and relative peak intensities must be compared qualitatively.

3. Results

3.1. Freshly polished sample

Iron, copper and nickel PEEM images from a region on the fresh polished sample containing all three mineral phases are presented in Fig. 2 alongside corresponding EDAX X-ray maps. The PEEM images (on the left of Fig. 2) indicate two major regions with either a dominant copper signal or a dominant iron signal, and four smaller regions with a high signal from nickel. Given the stoichiometry of the three minerals investigated here, the high copper region can be identified as chalcopyrite, the high iron region as pyrrhotite, and the three high nickel regions as pentlandite. This initial identification is confirmed with the EDAX X-ray maps (Fig. 2, right). The stoichiometry of the regions analysed (from the acquired EDAX spectra) is as follows: pentlandite $Ni_4Fe_4S_8$; pyrrhotite Fe_7S_8; chalcopyrite $CuFeS_2$.

The PEEM images in Fig. 2 were used to extract TEY NEXAFS spectra of the metals of interest for the three mineral phases. Fig. 3 shows the Cu L_3 TEY NEXAFS spectrum from the chalcopyrite phase (Fig. 3, inset position A) and Ni L_3 TEY NEXAFS spectrum from the pentlandite phase (Fig. 3, inset position B) in the freshly polished sample. Fig. 3

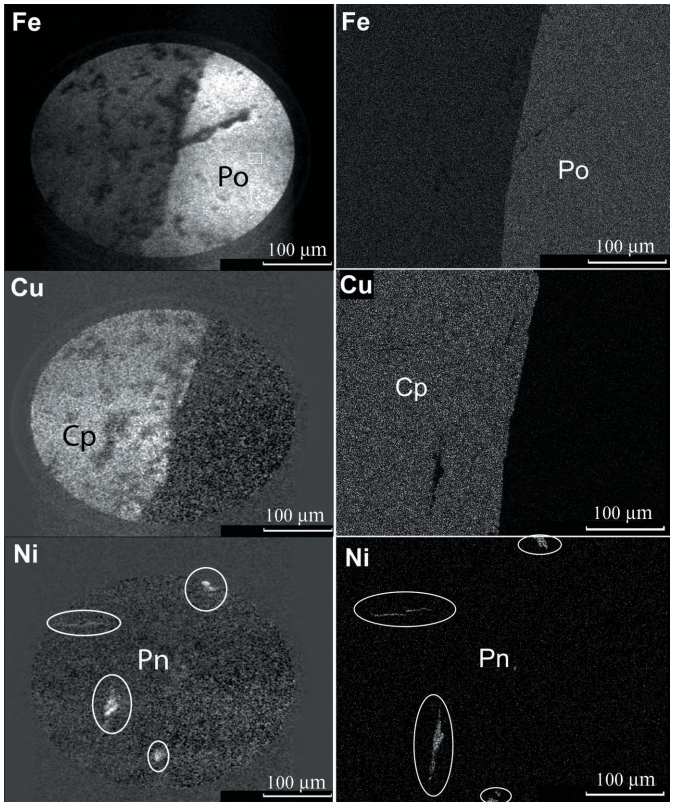

Figure 2
Iron, copper and nickel PEEM images (left) and EDAX X-ray maps (right) of the freshly polished sample. Each mineral phase is labelled: Po, pyrrhotite; Cp, chalcopyrite; Pn, pentlandite (regions highlighted within ovals).

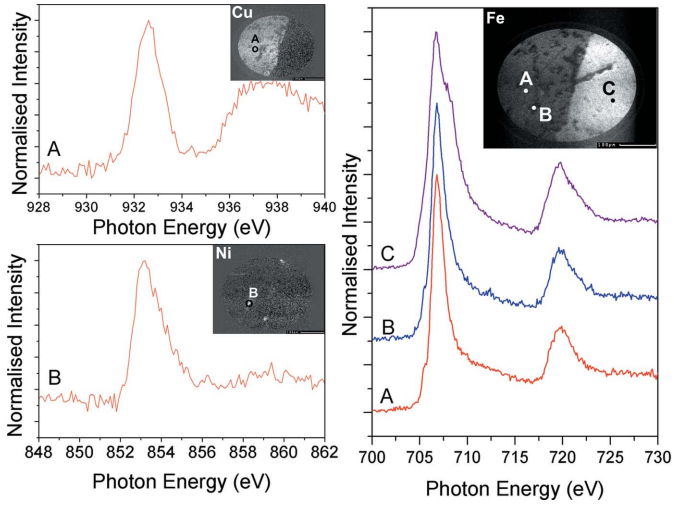

Figure 3
TEY NEXAFS spectra (polished sample) of Cu L_3 (top left) from chalcopyrite (inset point A), Ni L_3 (bottom left) from pentlandite (inset point B) and Fe $L_{2,3}$ (right) from chalcopyrite (point A), pentlandite (point B) and pyrrhotite (point C).

also shows Fe $L_{2,3}$ TEY NEXAFS spectra from points on each region: chalcopyrite (position A), pentlandite (position B) and pyrrhotite (position C). Image inserts indicate the points where each spectrum originated from the individual PEEM images. The Cu L_3 spectrum of the chalcopyrite in the polished sample shows a single peak at 932.6 eV corresponding to Cu(I) in chalcopyrite (Buckley *et al.*, 2007; Goh *et al.*, 2006*c*,*d*; Mikhlin *et al.*, 2004; Pearce *et al.*, 2006) and there is no evidence of a Cu(II) shoulder on the low binding energy side of the peak around 931 eV. There is a broad post-edge feature in the Cu L_3 spectrum at approximately 936–940 eV. This post-edge feature is enhanced owing to interference from the I_0 signal recorded on the Au grid, which was contaminated with copper. The interference does not affect the shape or position of the Cu L_3 peak. The fresh polished Ni L_3 spectrum has a single peak at 853.2 eV corresponding to Ni(II) as in pentlandite [853.2 eV (Goh *et al.*, 2006*b*)] with no clear indication of other peaks or shoulders.

The Fe $L_{2,3}$ spectra from all three regions are plotted on the right of Fig. 3, with the three spectra showing the characteristic Fe L_3 and L_2 peaks at 706.8 eV and 719.5 eV, respectively (Mikhlin *et al.*, 2004, 2005; Goh *et al.*, 2006*d*; Pearce *et al.*, 2006). Upon closer inspection the Fe L_3 peak of each mineral phase has some additional structure. The chalcopyrite and pentlandite phases on the freshly polished sample (Fig. 3, positions A and B, respectively) show one dominant Fe L_3 peak from the bulk minerals, but there is also a small almost fully resolved pre-edge feature at 705.5 eV. This pre-edge feature can be attributed to transitions of the Fe L_3 electrons to multiple unoccupied electron eigenstates [multiplets (Ikeno *et al.*, 2009)] just below the ionization threshold. It should be noted that the similarity in the Fe $L_{2,3}$ spectrum of pentlandite to that of chalcopyrite is not due to a contribution from chalcopyrite underlying the small pentlandite grains analysed. The TEY sampling depth (12 monolayers) is smaller than the EDAX detection depth; no Cu was detected in EDAX spectra

from the pentlandite regions of the sample, or in the pentlandite regions of the EDAX X-ray map shown in Fig. 2.

For the freshly polished pyrrhotite (Fig. 3, position C) there is some evidence of a pre-edge feature in addition to the peak at 706.8 eV, but the main additional structure in the Fe L_3 spectrum is a strong shoulder on the high binding energy side of the main peak at approximately 708 eV giving a line shape resembling that published by Mikhlin & Tomashevich (2005) and Goh *et al.* (2006*d*) for abraded pyrrhotite. The shoulder position corresponds to iron oxidation products (iron oxide and hydroxide) [708–709 eV (Mikhlin *et al.*, 2004, 2005; Goh *et al.*, 2006*d*; Mikhlin & Tomashevich, 2005)].

3.2. Oxidized sample

PEEM images collected from the polished sample exposed to pH 9 KOH for 30 min are presented in Fig. 4 with matching EDAX X-ray maps. Three large phases are distinguishable with higher concentrations of iron, copper and nickel comprising approximately a third of the image each. EDAX spectra confirmed the high iron, nickel and copper phases to be pyrrhotite (Fe_7S_8), pentlandite ($Ni_4Fe_4S_8$) and chalcopyrite ($CuFeS_2$), respectively.

After oxidation the Cu L_3 NEXAFS spectrum from the chalcopyrite phase (Fig. 5, position A) shows no variance from the Cu L_3 from the freshly polished sample, with a single peak at 932.6 eV from Cu(I) in chalcopyrite and no evidence of a Cu(II) shoulder. Like the Cu L_3 NEXAFS spectrum from the chalcopyrite phases, the Ni L_3 NEXAFS spectrum from oxidized pentlandite (Fig. 5, position B) phases show little variation from the fresh sample, with a single peak at 853.2 eV. The Fe $L_{2,3}$ NEXAFS spectra from the three different oxidized mineral phases (A, chalcopyrite; B, pentlandite; C, pyrrhotite) are also given in Fig. 5. The spectra from chalcopyrite and pentlandite are very similar to those obtained from the fresh polished sample, with a dominant L_3 peak at 706.8 eV. However, upon closer inspection, it appears that the L_3 peak is slightly broader for pentlandite, indicating the presence of a small amount of iron oxidation products. In addition, the pre-edge feature on the L_3 peak for pentlandite is not as well resolved as in the case of the freshly polished pentlandite. In contrast to pentlandite and chalcopyrite, where there are either minor or no indications of oxidation, the Fe $L_{2,3}$ spectrum of pyrrhotite has indications of significant further oxidation following exposure of the mineral sample of alkaline solution. The presence of the resolved 708.2 eV Fe L_3 peak is a clear indication that substantial oxidation has occurred on the pyrrhotite surface and the near-surface region. In addition, the L_2 Fe peak in this spectrum can also be seen to contain two components, one for bulk Fe in pyrrhotite and one for the oxidation products on the pyrrhotite surface. Pyrrhotite has oxidized extensively, especially when compared with pentlandite. The increased oxidation of pyrrhotite relative to the other minerals, indicated by the increased intensity of the peak at 708.2 eV, is as expected due to the high reactivity of pyrrhotite (Kolahdoozan, 2002; Miller *et al.*, 2005; Agar, 1991; Goh *et al.*, 2006*d*; Pratt *et al.*, 1994; Mycroft *et al.*, 1995; Buckley *et al.*, 1988; Buckley & Woods, 1985).

The presence of small amounts of iron oxidation products on pentlandite is confirmed by performing a subtraction of the fresh mineral spectrum from that of the oxidized mineral; the

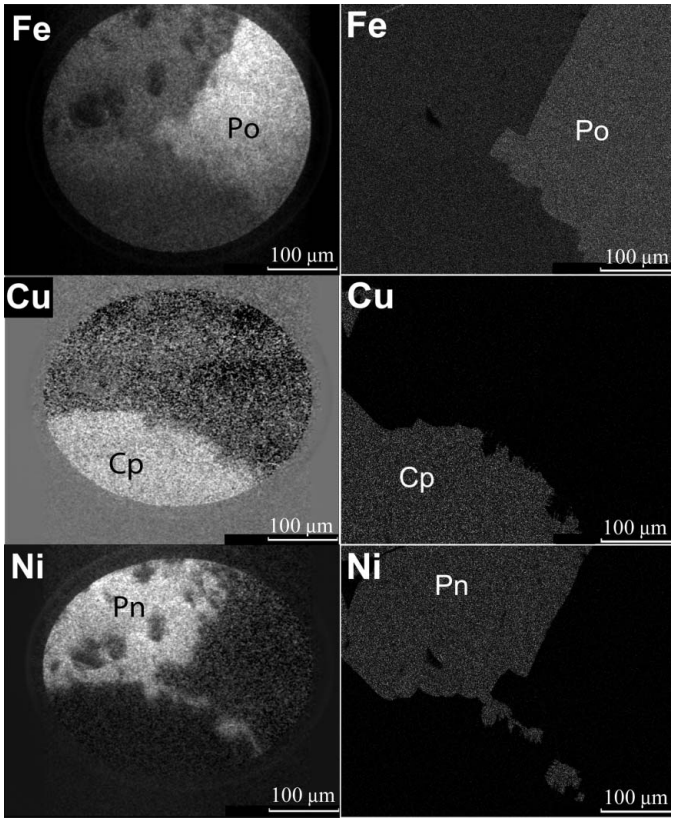

Figure 4
Iron, copper and nickel PEEM images (left) and EDAX X-ray maps (right) from the sample exposed to pH 9 KOH for 30 min. Each mineral phase is labelled: Po, pyrrhotite; Cp, chalcopyrite; Pn, pentlandite.

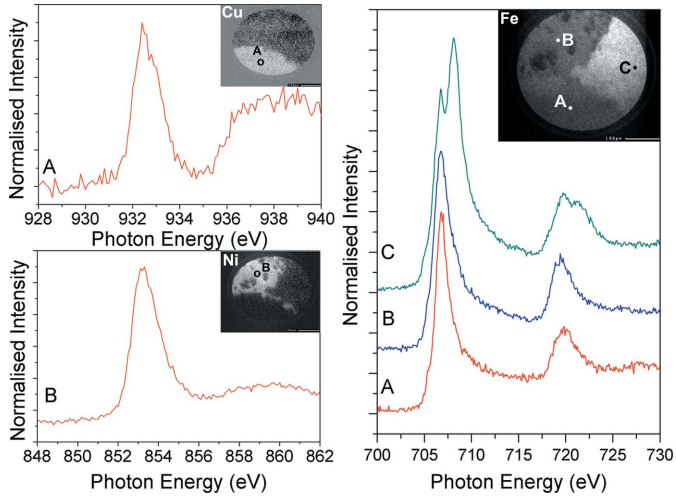

Figure 5
TEY NEXAFS spectra (oxidized sample) of Cu L_3 (top left) from chalcopyrite (inset point A), Ni L_3 (bottom left) from pentlandite (inset point B) and Fe $L_{2,3}$ (right) from chalcopyrite (point A), pentlandite (point B) and pyrrhotite (point C).

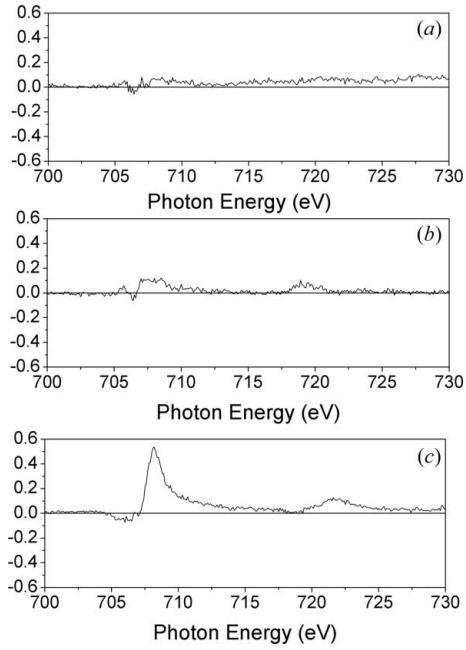

Figure 6
Subtraction TEY NEXAFS Fe $L_{2,3}$ spectra from (*a*) chalcopyrite (oxidized point A − fresh point A), (*b*) pentlandite (oxidized point B − fresh point B) and (*c*) pyrrhotite (oxidized point C − fresh point C).

subtraction spectra for all three mineral phases are given in Fig. 6. The residual from the subtraction is almost flat for chalcopyrite (Fig. 6*a*). However, the subtraction spectrum for pentlandite (Fig. 6*b*) has a small residual peak at approximately 708 eV, the position identified previously as Fe from iron hydroxide/oxide oxidation products. This observation indicates that pentlandite has undergone minor oxidation during the 30 min exposure to pH 9 solution. It would be expected that any spectral indication of oxidation of chalcopyrite and pentlandite would appear in the Fe $L_{3,2}$ spectrum as iron will oxidize preferentially over copper in chalcopyrite, and over nickel in pentlandite (Yin *et al.*, 1995; Buckley *et al.*, 1985; Buckley & Woods, 1984, 1991; Velasquez *et al.*, 2005; Legrand *et al.*, 1997; Richardson & Vaughan, 1989). The indications for the presence of oxidation products on the pyrrhotite surface do not require spectral subtraction for elucidation. However, the subtraction has been performed for the two pyrrhotite surfaces (fresh and oxidized) and this spectrum is given in Fig. 6(*c*) along with those for the two other minerals.

The oxidation of the pyrrhotite phase has been further investigated by extracting the Fe $L_{2,3}$ NEXAFS spectrum of pyrrhotite from near the phase boundary (position D) and comparing this with the spectrum extracted from the image point far from the phase boundary (position C). These spectra are compared in Fig. 7, along with a subtraction spectrum of the near phase boundary spectrum from the far-from phase boundary spectrum. This type of NEXAFS spectral comparison is only possible with PEEM. The spectrum from near the phase boundary has a larger contribution from the L_3 peak of Fe in pyrrhotite (706 eV); the degree of oxidation of pyrrhotite is reduced the closer to the phase boundary one probes.

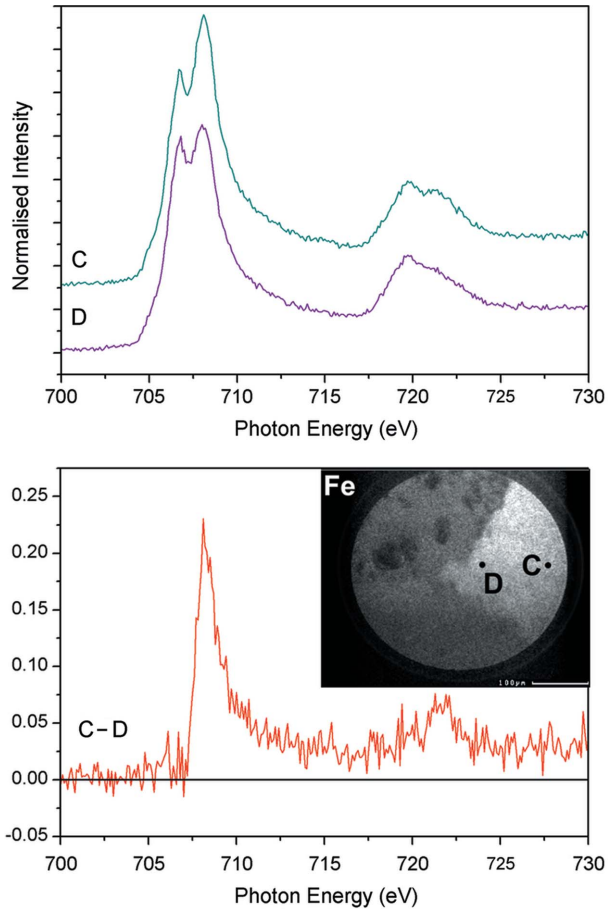

Figure 7
Comparison of TEY NEXAFS Fe $L_{2,3}$ spectra from oxidized pyrrhotite, far from the phase boundary (C), near the phase boundary (D) and the subtraction spectrum (C − D).

3.3. ToF-SIMS comparison

The TEY NEXAFS spectra collected in this study are sensitive to the mineral composition and coordination of metal atoms in the surface and near-surface region (*e.g.* the maximum depth probed was up to 12 monolayers). To get a picture of what is occurring on the very top surface layer (one to three monolayers), one has to use a probe of surface composition with higher surface selectivity. ToF-SIMS is one such probe: it provides compositional maps and can be used to compare surfaces before and after surface treatments. However, the higher degree of surface selectivity comes at a price: there is no spectral information, only mass information.

ToF-SIMS images from a freshly polished composite sample of chalcopyrite, pyrrhotite and pentlandite are presented in Fig. 8, with individual images constructed from the Cu, Fe and Ni mass peaks being combined to give a fourth overlay image that indicates the three different mineral phases (red, pyrrhotite; blue, pentlandite; green, chalcopyrite). The sample region is different from that analysed using PEEM but still contains the same three mineral phases in intimate contact. The signal from iron is present across the surface, which is to be expected given that iron is a major component of all three minerals. Also expected is the occurrence of nickel only in

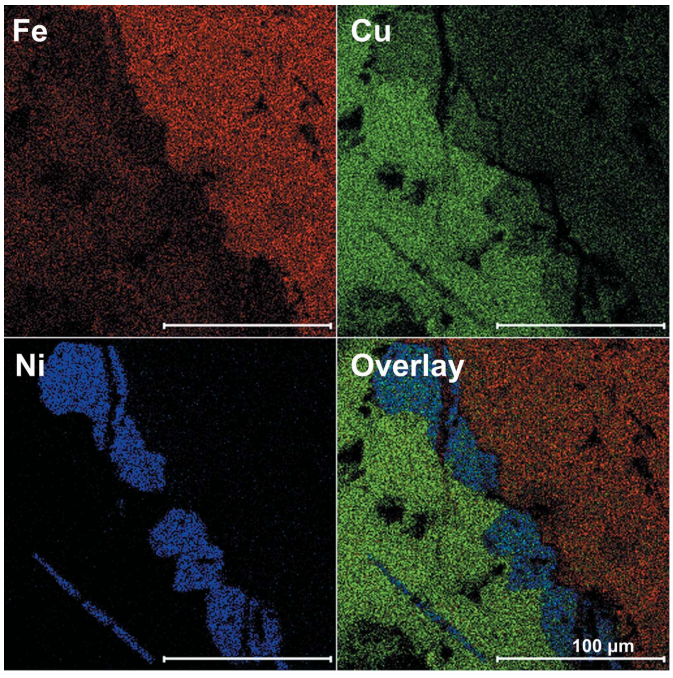

Figure 8
Cu, Ni and Fe and composite ToF-SIMS images from a polished composite sample containing chalcopyrite, pyrrhotite and pentlandite.

regions that can be identified as pentlandite; pyrrhotite and chalcopyrite contain no nickel. However, the signal from copper is seen across all three mineral phases, despite the fact that the bulk composition of the pyrrhotite and pentlandite indicates no copper. This is also in contrast to the PEEM images displayed in Fig. 2. The explanation for the disagreement most likely lies in the depth of sampling of ToF-SIMS and PEEM; ToF-SIMS will see primarily the first monolayer of material on the polished surface whereas PEEM sees up to 12 monolayers into the surface layer. Copper is observed on the surfaces of the pentlandite and pyrrhotite phases after polishing. It is likely that the layer of copper observed in the ToF-SIMS spectra is very thin and has arisen as a result of copper activation [uptake of dissolved copper into mineral surfaces (Finkelstein, 1997)] from copper liberated into the polishing slurry from the chalcopyrite region of the sample.

The ToF-SIMS ion images in Fig. 8 clearly allow one to designate regions of different mineralogy in the sample. Of more use for this investigation are the normalized peak intensities from positive and negative ions collected during the ToF-SIMS analysis. These mass peak intensities are plotted in Figs. 9, 10 and 11 (top, positive ions; bottom, negative ions) for chalcopyrite, pentlandite and pyrrhotite, respectively. The major mass peaks of interest are Fe, Cu, Si, Ni (positive ions), and S, S_n (n = 2–5), C and O (negative ions). The data in each figure include the normalized mass peak intensities before and after the freshly polished surface has been exposed to the pH 9 solution, *i.e.* before and after solution oxidation.

The ToF-SIMS data for chalcopyrite (Fig. 9) indicate that the solution oxidation has resulted in a statistically significant increase in iron and oxygen, and a statistically significant decrease in the amount of copper and sulfur. The insert in the

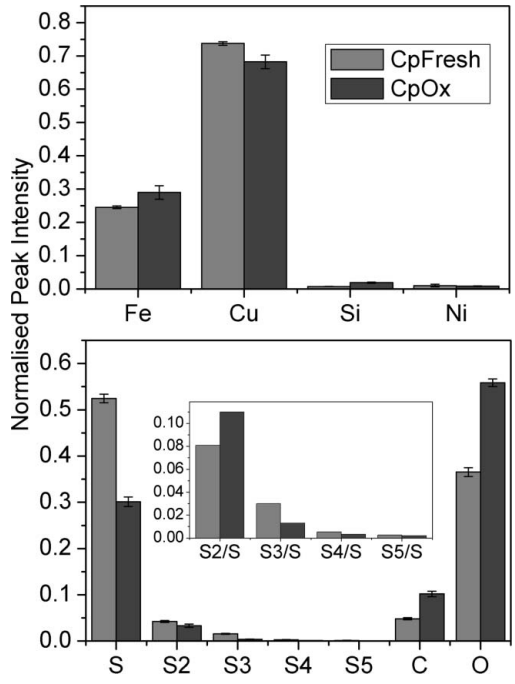

Figure 9
Normalized peak intensities from positive (top) and negative (bottom) ion ToF-SIMS of freshly polished and oxidized chalcopyrite. The inset in the negative-ion graph is an expansion of the sulfur species peak intensities. Light grey, freshly polished; dark grey, oxidized in pH 9 solution. Error bars represent the statistically significant confidence intervals (P = 95%) for each mass signal.

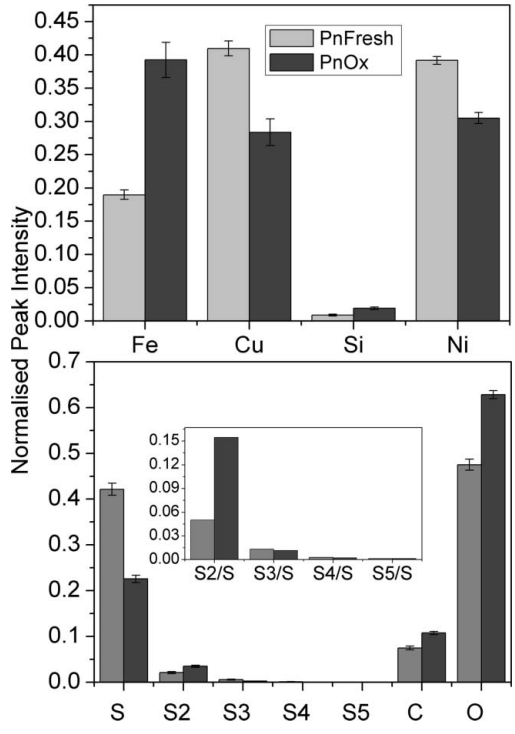

Figure 10
Normalized peak intensities from positive (top) and negative (bottom) ion ToF-SIMS of freshly polished and oxidized pentlandite. The inset in the negative-ion graph is an expansion of the sulfur species peak intensities. Light grey, freshly polished; dark grey, oxidized in pH 9 solution. Error bars represent the statistically significant confidence intervals (P = 95%) for each mass signal.

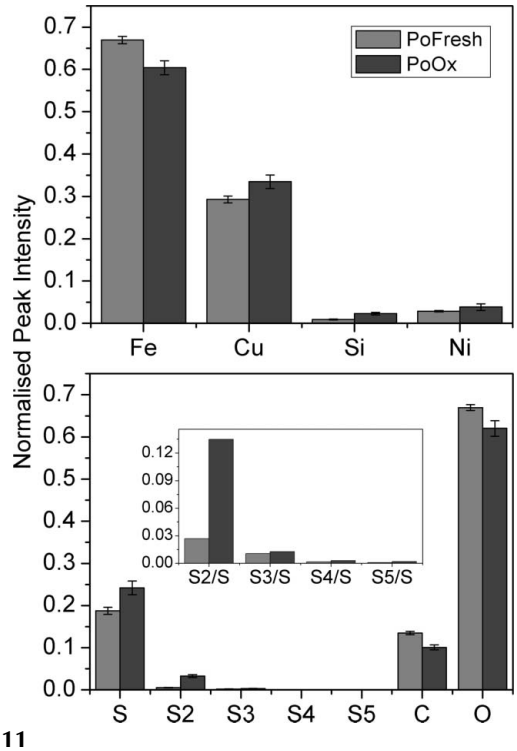

Figure 11
Normalized peak intensities from positive (top) and negative (bottom) ion ToF-SIMS of freshly polished and oxidized pyrrhotite. The inset in the negative-ion graph is an expansion of the sulfur species peak intensities. Light grey, freshly polished; dark grey, oxidized in pH 9 solution. Error bars represent the statistically significant confidence intervals (P = 95%) for each mass signal.

negative-ion spectrum in Fig. 9 shows different length sulfur chains normalized to the total sulfur. There was also an increase in the amount of S_2 produced at the chalcopyrite surface after oxidation as can be seen from the insert. These observations are consistent with mild oxidation of the chalcopyrite surface, with the production of iron hydroxide products, release of copper into solution, and the formation of surface sulfur species, such as disulfide and polysulfide (Acres *et al.*, 2010*a*; Buckley & Woods, 1984). An almost identical picture is generated for the development of the pentlandite surface when the data in Fig. 10 are inspected. The data in the figure indicate that iron and oxygen increase, while nickel and sulfur decrease (along with an increase in S_2, seen clearly in the insert in Fig. 10), again consistent with mild oxidation of the pentlandite surface. The data for pentlandite and chalcopyrite indicate that oxidation is occurring for these two mineral phases during exposure to pH 9 solution. Mild oxidation of chalcopyrite or pentlandite in air or alkaline solution produces a surface rich in polysulfides and some iron hydroxides (Buckley & Woods, 1984; Legrand *et al.*, 1997, 2005; Buckley & Woods, 1991; Richardson & Vaughan, 1989; Buckley *et al.*, 1985; Mielczarski *et al.*, 1996; Todd *et al.*, 2003). Surface polysulfides are the species responsible for hydrophobicity in the absence of collectors (Hayes *et al.*, 1987; Zachwieja *et al.*, 1989; Fairthorne *et al.*, 1997; Senior & Trahar, 1991). The oxidation of both minerals observed here is restricted to the first few monolayers of the surface. However, it is likely that the oxidation does penetrate further into the surface region, as indications of minor oxidation were also seen in the Fe NEXAFS spectrum of pentlandite presented in Fig. 5.

The ToF-SIMS data for pyrrhotite are given in Fig. 11. As with the previous two mineral phases, there are a number of differences in the normalized intensity of some positive and negative ions. However, there are a number of key differences. First, the amount of iron and oxygen on the pyrrhotite surface has actually decreased, albeit only slightly, and for the mineral that had the largest initial signals for these atoms at the surface. This is accompanied by an increase in copper and an increase in sulfur (pyrrhotite is the only phase to indicate an increase in sulfur at the surface following oxidation). Another point of note from the data in Fig. 11 is the increase in all sulfur polymer fragments (S_2, S_3, S_4 and S_5; see Fig. 11 insert). The data indicate that the surface of pyrrhotite has extensive amounts of sulfur oxidation products, increased copper activation and a small decrease in iron oxidation products. The last piece of information needs to be taken in the context of the depth of analysis of the ToF-SIMS experiments (top few monolayers). The PEEM data in Fig. 5 indicated clearly that there was a significant increase in the amount of iron hydroxide in the top 12 monolayers of the surface following oxidation. The oxidation of pyrrhotite has resulted in a significant degree of iron oxidation that penetrates into the near-surface region, and has left an outermost surface layer (the top one to three monolayers) rich in polysulfides, with evidence of extensive copper activation.

4. Discussion

Surface changes during oxidation are crucial to flotation and are different for mixtures of minerals compared with single minerals owing to processes such as inter-mineral galvanic interactions or the adsorption of metal ions rendering the surface 'active' for collectors (Yelloji Rao & Natarajan, 1989; Ekmekçi & Demirel, 1997; Holmes & Crundwell, 1995; Nakazawa & Iwasaki, 1986; Kelebek & Nanthakumar, 2007; Cheng *et al.*, 1999; Pozzo & Iwasaki, 1988; Yoon *et al.*, 1995; Harmer *et al.*, 2008). Galvanic interactions between minerals occur due to differences in mineral rest potentials. Due to their semiconducting nature, when two sulfides are in electrical contact in solution a galvanic pair can be created where the mineral with the higher rest potential will act as a cathode and the mineral with the lower rest potential forming the anode. For the minerals studied in this investigation the order of rest potentials is chalcopyrite > pentlandite > pyrrhotite (Cheng *et al.*, 1999; Bozkurt *et al.*, 1998; Buswell *et al.*, 2002; Khan & Kelebek, 2004; Ralston, 1991).

Preferential oxidation of pyrrhotite with minimal alteration of chalcopyrite and minor oxidation of pentlandite is in agreement with the literature on galvanic interactions, where the cathode is protected while the oxidation at the anode is accelerated (Ekmekçi & Demirel, 1997; Yelloji Rao & Natarajan, 1989). Given the relative rest potentials of the three minerals, pyrrhotite will act as an anode in the three

mineral coupling, with chalcopyrite as the cathode (Cheng *et al.*, 1999; Bozkurt *et al.*, 1998; Buswell *et al.*, 2002; Khan & Kelebek, 2004; Ralston, 1991; Miller *et al.*, 2005). Minerals with intermediate rest potentials in a multi-mineral coupling may act either as a cathode or anode depending on its rest potential (Cheng *et al.*, 1999; Pozzo & Iwasaki, 1988). In this case the lack of major oxidation of pentlandite indicates that it is most likely acting cathodically.

Although galvanic interaction can explain the majority of observations from the PEEM and ToF-SIMS data, it cannot explain the greater oxidation of pyrrhotite away from an interface relative to near the interface. For regions of pyrrhotite with the same composition, the galvanic interaction 'off interface' should be the same as 'near interface'. EDAX measurements showed no variance in the composition of the pyrrhotite along the mineral toward the phase boundary. One plausible explanation for the observed difference is that the solution composition above the near and far regions of the pyrrhotite was slightly different during the oxidation. The sample was in a non-stirred solution, with the possible result that a chemical gradient in solution was established during the oxidation (*e.g.* the persistence of localized dissolution species in the interfacial areas). This possibility will be explored in future studies with immersion/oxidation being performed in a flowing/stirred solution.

Finally, the observation of copper activation on the freshly polished surface indicates that care must be taken if highly surface-sensitive measurements are to be made on a surface prepared by polishing. Since PEEM has a more significant probe depth compared with ToF-SIMS, the presence of copper at the surface (one to three monolayers) would not have as dramatic an influence on the acquired spectra. This would actually appear to be an advantage of PEEM of polished surfaces when compared with ToF-SIMS.

5. Conclusions

PEEM has been successfully employed to image a heterogeneous mineral (before and after solution oxidation) containing pyrrhotite, pentlandite and chalcopyrite and identify regions where these mineral phases are in intimate contact. From these PEEM images, each mineral phase has been individually probed using TEY NEXAFS. The NEXAFS results show the pyrrhotite phase has oxidized preferentially to the chalcopyrite and pentlandite and that oxidation occurs at a greater rate away from an interface. ToF-SIMS results show that some oxidation of the pentlandite and chalcopyrite phases has occurred, but, since there is only minor indications of oxidation products in the NEXAFS spectra for pentlandite and almost no indication of oxidation for chalcopyrite, this oxidation is only superficial in terms of the depth probed by TEY, and when compared with the oxidation observed in pyrrhotite. Copper has been observed on all phases of the freshly polished sample with ToF-SIMS, indicating that liberated copper present in the polishing slurry has adsorbed and reacted with the other phases (copper activation). Nevertheless, polishing is a suitable preparation method for PEEM analysis owing to the increased depth probed for PEEM as compared with ToF-SIMS.

The authors would like to acknowledge financial support from the Australian Research Council Linkage Scheme (AMSRI, LP0667828), AMIRA International, and the sponsors of AMIRA International Project P924: BHP/Billiton, Rio Tinto, Orica Explosives, Anglo Platinum, Xstrata Technology, Freeport McMoran and AREVA NC. The authors would also like to thank Associate Professor Bill Skinner (Ian Wark Research Institute, University of South Australia) for supplying the mineral samples. Synchrotron PEEM analysis was conducted at the National Synchrotron Radiation Research Centre (NSRRC), Taiwan, and the authors would like to thank the BL05B2 team for their assistance.

References

Acres, R. G., Harmer, S. L. & Beattie, D. A. (2010*a*). *Int. J. Miner. Process.* **94**, 43–51.
Acres, R. G., Harmer, S. L. & Beattie, D. A. (2010*b*). *Miner. Eng.* In the press.
Agar, G. E. (1991). *Int. J. Miner. Process.* **33**, 1–19.
Blanchard, P. E. R., Grosvenor, A. P., Cavell, R. G. & Mar, A. (2008). *Chem. Mater.* **20**, 7081–7088.
Bozkurt, V., Xu, Z. & Finch, J. A. (1998). *Int. J. Miner. Process.* **52**, 203–214.
Bozkurt, V., Xu, Z. & Finch, J. A. (1999). *Can. Metall. Q.* **38**, 105–112.
Brion, D. (1980). *Applic. Surf. Sci* **5**, 133–152.
Buckley, A. N. (1994). *Colloids Surf. A*, **93**, 159–172.
Buckley, A. N., Goh, S. W., Lamb, R. N. & Woods, R. (2003). *Int. J. Miner. Process.* **72**, 163–174.
Buckley, A. N., Hamilton, I. C. & Woods, R. (1985). *Developments in Mineral Processing Flotation of Sulfide Minerals*, edited by K. S. E. Forssberg, pp. 41–60. Amsterdam/New York: Elsevier.
Buckley, A. N., Hamilton, I. C. & Woods, R. (1988). *Proceedings of the International Symposium on Electrochemistry in Mineral and Metal Processing II*, edited by P. E. Richardson and R. Woods, pp. 234–246. Pennington: The Electrochemical Society.
Buckley, A. N., Skinner, W. M., Harmer, S. L., Pring, A., Lamb, R. N., Fan, L.-J. & Yang, Y.-W. (2007). *Can. J. Chem.* **85**, 767–781.
Buckley, A. N. & Woods, R. (1984). *Aust. J. Chem.* **37**, 2403–2413.
Buckley, A. N. & Woods, R. (1985). *Applic. Surf. Sci.* **22–23**, 280–287.
Buckley, A. N. & Woods, R. (1991). *Surf. Interface Anal.* **17**, 675–680.
Buswell, A. M., Bradshaw, D. J., Harris, P. J. & Ekmekci, Z. (2002). *Miner. Eng.* **15**, 395–404.
Cheng, X., Iwasaki, I. & Smith, K. A. (1999). *Miner. Metall. Process.* **16**, 69–71.
Ekmekçi, Z. & Demirel, H. (1997). *Int. J. Miner. Process.* **52**, 31–48.
Fairthorne, G., Fornasiero, D. & Ralston, J. (1997). *Int. J. Miner. Process.* **49**, 31–48.
Finkelstein, N. P. (1997). *Int. J. Miner. Process.* **52**, 81–120.
Goh, S., Buckley, A., Lamb, R., Fan, L.-J., Jang, L.-Y. & Yang, Y.-W. (2006*a*). *Phys. Chem. Miner.* **33**, 445–456.
Goh, S., Buckley, A., Lamb, R., Skinner, W., Pring, A., Wang, H., Fan, L.-J., Jang, L.-Y., Lai, L.-J. & Yang, Y.-W. (2006*b*). *Phys. Chem. Miner.* **33**, 98–105.
Goh, S. W., Buckley, A. N. & Lamb, R. N. (2006*c*). *Miner. Eng.* **19**, 204–208.
Goh, S. W., Buckley, A. N., Lamb, R. N., Rosenberg, R. A. & Moran, D. (2006*d*). *Geochim. Cosmochim. Acta*, **70**, 2210–2228.
Grano, S. R., Sollaart, M., Skinner, W., Prestidge, C. A. & Ralston, J. (1997). *Int. J. Miner. Process.* **50**, 1–26.
Harmer, S. L., Mierczynska-Vasilev, A., Beattie, D. A. & Shapter, J. G. (2008). *Miner. Eng.* **21**, 1005–1012.

Harmer, S. L., Pratt, A. R., Nesbitt, H. W. & Fleet, M. E. (2005). *Can. Miner.* **43**, 1619–1630.
Harmer, S. L., Pratt, A. R., Nesbitt, W. H. & Fleet, M. E. (2004). *Am. Miner.* **89**, 1026–1032.
Harmer, S. L., Skinner, W. M., Buckley, A. N. & Fan, L.-J. (2009). *Surf. Sci.* **603**, 537–545.
Harmer, S. L., Thomas, J. E., Fornasiero, D. & Gerson, A. R. (2006). *Geochim. Cosmochim. Acta*, **70**, 4392–4402.
Hayes, R. A., Price, D. M., Ralston, J. & Smith, R. W. (1987). *Miner. Process. Extr. Metall. Rev.* **2**, 203–234.
Heiskanen, K., Kirjavainen, V. & Laapas, H. (1991). *Int. J. Miner. Process.* **33**, 263–274.
Holmes, P. R. & Crundwell, F. K. (1995). *Hydrometallurgy*, **39**, 353–375.
Ikeno, H., De Groot, F. M. F., Stavitski, E. & Tanaka, I. (2009). *J. Phys. Condens. Matter*, **21**, 104208.
Kelebek, S. (1993). *XVIII International Mineral Processing Congress.* Sydney: Australasian Institute of Mining and Metallurgy.
Kelebek, S. & Nanthakumar, B. (2007). *Int. J. Miner. Process.* **84**, 69–80.
Kelebek, S., Wells, P. F. & Fekete, S. O. (1996). *Can. Metall. Q.* **35**, 329–336.
Khan, A. & Kelebek, S. (2004). *J. Appl. Electrochem.* **34**, 849–856.
Khmeleva, T. N., Georgiev, T. V., Jasieniak, M., Skinner, W. M. & Beattie, D. A. (2005). *Surf. Interface Anal.* **37**, 699–709.
Kolahdoozan, M. (2002). *Int. J. Eng. Sci.* **13**, 135–144.
Laajalehto, K., Kartio, I. & Suoninen, E. (1997). *Int. J. Miner. Process.* **51**, 163–170.
Legrand, D. L., Bancroft, G. M. & Nesbitt, H. W. (1997). *Int. J. Miner. Process.* **51**, 217–228.
Legrand, D. L., Bancroft, G. M. & Nesbitt, H. W. (2005). *Am. Miner.* **90**, 1042–1054.
Mielczarski, J. A., Cases, J. M., Alnot, M. & Ehrhardt, J. J. (1996). *Langmuir*, **12**, 2519–2530.
Mikhlin, Y. L., Tomashevich, Y. V., Asanov, I. P., Okotrub, A. V., Varnek, V. A. & Vyalikh, D. V. (2004). *Appl. Surf. Sci.* **225**, 395–409.
Mikhlin, Y. & Tomashevich, Y. (2005). *Phys. Chem. Miner.* **32**, 19–27.
Mikhlin, Y., Tomashevich, Y., Tauson, V., Vyalikh, D., Molodtsov, S. & Szargan, R. (2005). *J. Electron Spect. Rel. Phenom.* **142**, 83–88.
Miller, J. D., Li, J., Davidtz, J. C. & Vos, F. (2005). *Miner. Eng.* **18**, 855–865.
Mycroft, J. R., Nesbitt, H. W. & Pratt, A. R. (1995). *Geochim. Cosmochim. Acta*, **59**, 721–733.
Nakazawa, H. & Iwasaki, I. (1986). *Int. J. Miner. Process.* **18**, 203–215.
Newell, A. J. H., Bradshaw, D. J. & Harris, P. J. (2006). *Miner. Eng.* **19**, 675–686.
Parker, G. K., Woods, R. & Hope, G. A. (2005). *Proc. Electrochem. Soc.* **2004–18**, 104–115.
Pearce, C. I., Pattrick, R. A. D., Vaughan, D. J., Henderson, C. M. B. & van der Laan, G. (2006). *Geochim. Cosmochim. Acta*, **70**, 4635–4642.
Piantadosi, C., Jasieniak, M., Skinner, W. M. & Smart, R. S. C. (2000). *Miner. Eng.* **13**, 1377–1394.
Piantadosi, C. & Smart, R. S. C. (2002). *Int. J. Miner. Process.* **64**, 43–54.
Pozzo, R. L. & Iwasaki, I. (1988). *Proceedings of the International Symposium on Electrochemistry in Mineral and Metal Processing II*, edited by P. E. Richardson and R. Woods, pp. 66–83. Pennington: The Electrochemical Society.
Pratt, A. (2004). *Surf. Interface Anal.* **36**, 654–657.
Pratt, A. R., Franzreb, K. & McIntyre, N. S. (1998). *Surf. Interface Anal.* **26**, 869–871.
Pratt, A. R., Muir, I. J. & Nesbitt, H. W. (1994). *Geochim. Cosmochim. Acta*, **58**, 827–841.
Priest, C., Stevens, N., Sedev, R., Skinner, W. & Ralston, J. (2008). *J. Colloid Interface Sci.* **320**, 563–568.
Ralston, J. (1991). *Miner. Eng.* **4**, 859–878.
Richardson, S. & Vaughan, D. J. (1989). *Mineral. Mag.* **53**, 213–222.
Schmidt, O., Fazan, T. A., Morais, J. & Fecher, G. H. (2001). *Surf. Sci.* **482–485**, 568–573.
Senior, G. D. & Trahar, W. J. (1991). *Int. J. Miner. Process.* **33**, 321–341.
Senior, G. D., Trahar, W. J. & Guy, P. J. (1995). *Int. J. Miner. Process.* **43**, 209–234.
Smart, R. S. C., Amarantidis, J., Skinner, W., Prestidge, C. A., La Vanier, L. & Grano, S. (1998). *Scanning Microsc.* **12**, 553–583.
Smart, R. S. C., Jasieniak, M., Prince, K. E. & Skinner, W. M. (2000). *Miner. Eng.* **13**, 857–870.
Smith, A. D., Cressey, G., Schofield, P. F. & Cressey, B. A. (1998). *J. Synchrotron Rad.* **5**, 1108–1110.
Todd, E. C., Sherman, D. M. & Purton, J. A. (2003). *Geochim. Cosmochim. Acta*, **67**, 2137–2146.
Vaughan, D. J., Becker, U. & Wright, K. (1997). *Int. J. Miner. Process.* **51**, 1–14.
Velasquez, P., Leinen, D., Pascual, J., Ramos-Barrado, J. R., Grez, P., Gomez, H., Schrebler, R., Del Rio, R. & Cordova, R. (2005). *J. Phys. Chem. B*, **109**, 4977–4988.
Vickerman, J. C. (2001). *ToF-SIMS: Surface Analysis by Mass Spectrometry*, edited by J. C. Vickerman and D. Briggs, pp. 1–40. Chichester/Manchester: IM Publications.
Wills, B. A. & Napier-Munn, T. (2005). *Wills' Mineral Processing Technology*, 7th ed., pp. 267–352. Oxford: Butterworth-Heinemann.
Yelloji Rao, M. K. & Natarajan, K. A. (1989). *Int. J. Miner. Process.* **27**, 279–293.
Yin, Q., Kelsall, G. H., Vaughan, D. J. & England, K. E. R. (1995). *Geochim. Cosmochim. Acta*, **59**, 1091–1100.
Yin, Q., Vaughan, D. J., England, K. E. R., Kelsall, G. H. & Brandon, N. P. (2000). *J. Electrochem. Soc.* **147**, 2945–2951.
Yoon, R. H., Basilio, C. I., Marticorena, M. A., Kerr, A. N. & Stratton-Crawley, R. (1995). *Miner. Eng.* **8**, 807–816.
Zachwieja, J. B., McCarron, J. J., Walker, G. W. & Buckley, A. N. (1989). *J. Colloid Interface Sci.* **132**, 462–468.